Characterizing the Background Noise Level of Rotational Ground Motions on Earth

Andreas Brotzer[*1] , Heiner Igel[1] , Eléonore Stutzmann[2] , Jean-Paul Montagner[2] , Felix Bernauer[1] , Joachim Wassermann[1] , Rudolf Widmer-Schnidrig[3] , Chin-Jen Lin[4] , Sergey Kiselev[5] , Frank Vernon[6] , and Karl Ulrich Schreiber[7]

Abstract

The development of high-sensitive ground-motion instrumentation for Earth and planetary exploration is governed by so-called low-noise models, which characterize the minimum level of physical ground motions, observed across a very broad frequency range (0.1 mHz–100 Hz). For decades, broadband instruments for seismic translational ground-motion sensing allowed for observations down to the Earth's low-noise model. Knowing the lowermost noise level distribution across frequencies enabled not only to infer characteristics of Earth such as the ocean microseismic noise (microseisms) and seismic hum, but also to develop highly successful ambient seismic noise analysis techniques in seismology. Such a low-noise model currently does not exist for rotational ground motions. In the absence of a substantial observational database, we propose a preliminary rotational low-noise model (RLNM) for transverse rotations based on two main wavefield assumptions: the frequency range under investigation is dominated by surface-wave energy, and the employed phase velocity models for surface waves are representative. These assumptions hold, in particular, for a period range of about 2–50 s and lose validity towards long periods when constituents produced by atmospheric pressure dominate. Because noise levels of vertical and horizontal accelerations differ, we expect also different noise levels for transverse and vertical rotations. However, at this moment, we propose a common model for both types of rotations based on the transverse RLNM. We test our RLNM against available direct observations provided by two large-scale ring lasers (G-ring and ROMY) and array-derived rotations (Piñon Flats Observatory array, Gräfenberg array, and ROMY array). We propose this RLNM to be useful as guidance for the development of high-performance rotation instrumentation for seismic applications in a range of 2–50 s. Achieving broadband sensitivity below such a RLNM remains a challenging task, but one that has to be achieved.

Introduction

The concept of low-noise models is known in many scientific fields and characterizes the minimum background noise level for a certain measurement in a given environment. Noncoherent noise levels, thus nontransient signals, are commonly described by computing a power spectral density (PSD) across the relevant frequency bandwidth. Applied on seismic, or more general, physical ground motions, this reflects the minimal power of seismic or physical background motions expected on a planet per frequency band under the best observational circumstances. Therefore, a low-noise model sets the minimum threshold for observations of signals of interest. For translational seismic ground motions, more precisely acceleration, a new low- and high-noise model (NLNM and NHNM) has been presented by Peterson (1993) replacing the previous models by Brune and Oliver (1959). These models were based on the envelope of averaged PSDs computed for recordings of ground acceleration for a set of 75 global stations (Peterson,

1993). The NLNM still serves as a benchmark for instrumental self-noise level of translational seismic sensors to resolve observations of the lowermost expected signals. With the emergence of rotational observations in seismology due to new instrumentation developments, such as large-scale Sagnac interferometers, also referred to as ring lasers (Stedman et al., 1995; McLeod et al., 1998; Schreiber and Wells, 2023), and optical fibre gyroscopes (Bernauer et al., 2012, 2018), at the beginning of this century, a constant drive for improved instrumentation and application in seismology could be observed (e.g., Pancha et al., 2000; Igel et al., 2005; Wassermann et al., 2009; Schmelzbach et al., 2018; Kislov and Gravirov, 2021). Observations of three components of rotational ground motions complement classic observations of three components of translational ground motions. In general, a deformable elastic medium has 12 independent degrees of freedom (three for translation, three for rotation and six for strain; e.g. Aki and Richards, 2002). Colocated seismometers and rotational sensors, with three components each (6C station), enable the application of new processing techniques (e.g., Igel et al., 2007; Sollberger et al., 2020), in particular, for field deployment (Yuan et al., 2020), to better understand seismic wavefields and the subsurface. Resulting benefits comprise, for instance, general wavefield decomposition (Sollberger et al., 2020), ambient noise analysis (Hadziioannou et al., 2012; Tanimoto et al., 2015), site characterization (Singh et al., 2020; Keil et al., 2021), local measurement of anisotropy (Noe et al., 2022; Tang et al., 2023), improved structural health monitoring (Zembaty et al., 2021; Liao et al., 2022), teleseismic and eigenmode observations (e.g., Igel et al., 2011; Lin et al., 2011; Nader et al., 2015), enhanced moment tensor inversion (Donner et al., 2016), dynamic tilt correction of horizontal components of seismometers (e.g., Bernauer et al., 2020), especially for ocean-bottom seismometers (Lindner et al., 2017), as well as structural health monitoring (Guéguen and Astorga, 2021). Currently, a variety of rotational sensors are operated and developed, such as large-scale ring lasers (e.g., Schreiber et al., 2006; Ortolan et al., 2016; Igel et al., 2021), fibre-optic gyroscopes (e.g., Bernauer et al., 2018), mechanical beam balances (e.g., McCann et al., 2021; Venkateswara et al., 2021), or liquid-based sensors (Leugoud and Kharlamov, 2012). However, to fully exploit the aforementioned variety of benefits for seismological applications, portable rotational sensors with improved sensitivity across a wide frequency range are required. To benchmark this instrumentation development, knowing the rotational low-noise model (RLNM) for Earth (and eventually other extraterrestrial bodies) is crucial.

We describe the employed methodology in the Methodology section, all data used for comparison with the theoretical low-noise model for rotations in the Observational Data section, and our results in the Results section. Supporting materials are appended.

Methodology

The NLNM by Peterson (1993) for vertical acceleration is inferred from global observations. Because of a current shortage of permanently operated rotational sensors with high sensitivity, we chose a theoretical approach to convert the NLNM for vertical accelerations to obtain a theoretical RLNM for transverse rotations on Earth.

Translation to rotation

To convert translations to rotations, we use known relations for plane waves in linear elasticity, introducing rotations at the free surface (e.g., Cochard et al., 2006). The rotation rate $\dot{\vec{\Omega}}$ is generally defined as follows:

$$\dot{\vec{\Omega}}(\vec{r},t) = \frac{1}{2}\frac{\partial}{\partial t}(\vec{\nabla} \times \vec{u}(\vec{r},t)), \tag{1}$$

in which $\vec{u}(\vec{r},t)$ is the seismic displacement, at the location $\vec{r}$ and time t.

For SH-polarized waves (Love waves), the vertical rotation rate $\dot{\Omega}_Z$ is related via the horizontal Love phase velocity c_L with the transverse acceleration $\ddot{u}_T$,

$$\dot{\Omega}_Z = -\frac{1}{2}\frac{\ddot{u}_T}{c_L}. \tag{2}$$

For SV-polarized waves (Rayleigh waves), the transverse rotation rate $\dot{\Omega}_T$ is related via the horizontal Rayleigh phase velocity c_R with the vertical acceleration $\ddot{u}_Z$,

$$\dot{\Omega}_T = \frac{\ddot{u}_Z}{c_R}. \tag{3}$$

Equations (2) and (3) have been described in the previous literature (e.g., McLeod et al., 1998; Pancha et al., 2000; Igel et al., 2005; Lin et al., 2011; Belfi et al., 2012). A more detailed derivation is provided in the supplemental material available to this article (Appendix 6).

The existing NLNM for vertical translations as PSD (Peterson, 1993), commonly encountered as relative decibel units, enables an estimate of a low-noise model for (transverse) rotations using equation (3) according to the following equation:

$$\mathrm{PSD}_\Omega(T) = (\sqrt{10^{\mathrm{PSD}_a^{\mathrm{dB}}(T)/10}}/c_{\mathrm{ph},R}(T))^2 \text{ with}$$

$$[\mathrm{PSD}_\Omega(T)] = \frac{\mathrm{rad}^2}{\mathrm{s}^2 \, \mathrm{Hz}}, \tag{4}$$

in which T denotes the period, and $c_{\mathrm{ph},R}(T)$ is the dispersive Rayleigh phase velocity. See supplemental material for more details. However, this approach relies on two essential assumptions:

1. The power of the vertical acceleration in the NLNM is attributed dominantly to fundamental mode Rayleigh waves, at least for a range of 2–200 s in which this assumption approximately holds; and

2. the global, dispersive Rayleigh phase velocity structure (for the fundamental mode) is known or modeled as a distribution or maximum-likelihood curve.

These assumptions and their consequences are discussed in detail in the Discussion. In this article, figures are consistently discussed in terms of power or rather power density ($\frac{\text{rad}^2}{\text{s}^2\,\text{Hz}}$) of rotational rate ($\frac{\text{rad}}{\text{s}}$) observations and across periods instead of frequencies.

Global phase velocities
We used the global *S*-wave velocity model obtained by Haned *et al.* (2016), hereafter called HUM2. This model was derived from the inversion of path average Rayleigh-wave group velocities measured on empirical Green functions in the period range from 32 to 246 s. The crustal part of the model is based on Crust1.0 (Laske *et al.*, 2013) laterally smoothed with a correlation length of 800 km, which corresponds to the resolution of the mantle part of the model. The lateral resolution of this model is sufficient for investigating the RLNM. Phase velocities were then computed on a grid of 1° × 1°, following Saito (1988) and using the model HUM2. To infer the global phase velocities for fundamental mode, dispersive Rayleigh waves, two processing steps were applied:

1. the sampling density at the pole regions has been reduced by introducing the minimum distance (4° ≈ 444 km) between sampling locations along each latitude, to avoid a regional bias. The resampled locations are shown in Figure S6b; and
2. sampling locations in the oceans are neglected using a geographic continent-ocean mask (Todd, 2020) to satisfy the assumption of observing dominantly fundamental mode Rayleigh-wave energy and use comparable velocity profiles for continental crust only.

The sampled locations to extract phase velocities, based on the HUM2 model (Haned *et al.*, 2016), are shown in Figure S6a. A probability density distribution of all 1542 extracted phase velocities within 2–200 s are shown in Figure 1b as a probability density distribution. As expected, high variance of Rayleigh phase velocities is observed for shorter periods (below 10 s), which are mostly sensitive to the large lateral variations of the crust and lithosphere. Toward longer periods, phase velocities display less lateral variations.

Observational Data
To validate the proposed theoretical RLNM, we compare it with available direct observations of large-scale ring lasers as well as array-derived rotational ground motions based on three seismic arrays with different apertures, thus period ranges. All data cover the entire year of 2019 and are described in detail hereafter. An explicit exclusion of seismic events has

been neglected and dominating seismic noise is assumed across the long observation period justifying PSD computation.

Statistical single-station validation
To evaluate the model in a first step, we chose a statistical approach to infer many local rotational models using vertical acceleration recordings and the local Rayleigh-wave phase velocities computed for the HUM2 model (Haned *et al.*, 2016). Data of the entire year of 2019 of 120 globally distributed seismic stations (Fig. S6a) are used to infer mean and median PSDs for each station. An estimate of the local PSD for rotational ground motions is obtained using the local Rayleigh-wave phase velocities, which are interpolated at each station location (Fig. 3e).

Array-derived rotations
Rotational ground motions can be inferred from well-designed seismic arrays (Huang, 2003; Suryanto *et al.*, 2006; Spudich and Fletcher, 2008). Three-component array-derived rotations (ADR) are computed for 2019 for three different seismic arrays: (1) the ROMY array (RMY) surrounding the site of the Geophysical Observatory in Fürstenfeldbruck, Germany; (2) a subset of the Piñon Flats Observatory array (PFO array) in California, U.S.A.; and (3) a subset of the Gräfenberg array (GRF) located in southeastern Germany.

For RMY, an inner array comprising four stations (FUR, FFB1, FBB2, and FFB3) and an outer array with six stations, using FUR as a central station, is deployed (see Fig. S1b). The station distribution of the selected seismic arrays is shown in Figure S1 with the arrays' aperture indicated. The frequency range for array derived rotations is limited,

$$\frac{0.03c}{a} < f < \frac{0.25c}{a}, \tag{5}$$

in which the lower limit depends on the array's aperture *a* and the local apparent horizontal seismic phase velocity *c* (Spudich and Fletcher, 2008; Poppeliers and Evans, 2015). Poppeliers and Evans (2015) set the value of 0.03 for the lower frequency limitation based on amplitude measurement uncertainty and interstation distances, both being crucial for gradient calculation. For the PFO array, Donner *et al.* (2017) adjusted the lower frequency limit,

$$\frac{0.00238c}{a} < f < \frac{0.25c}{a}, \tag{6}$$

based on a re-evaluation of the amplitude uncertainty of the arrays' sensors. Table 1 lists the applied limits for the three arrays. Hourly PSDs are computed for each of the three components (Figs. S2–S5). As a statistical representation, a median PSD is generally compared with the proposed RLNM.
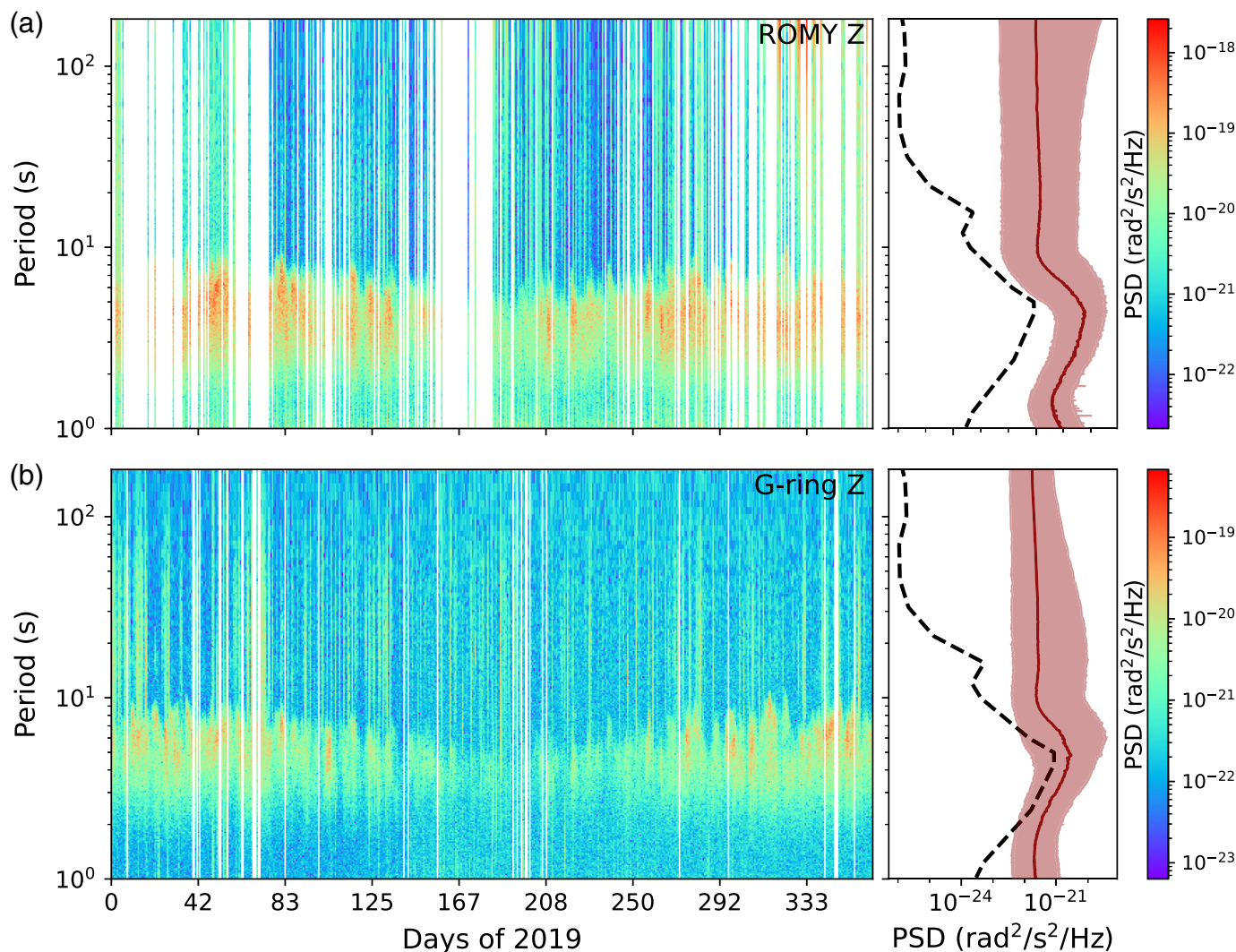
Ring laser observations
Direct measurements of vertical ground rotations are provided by permanent, large-scale ring lasers (= optical Sagnac
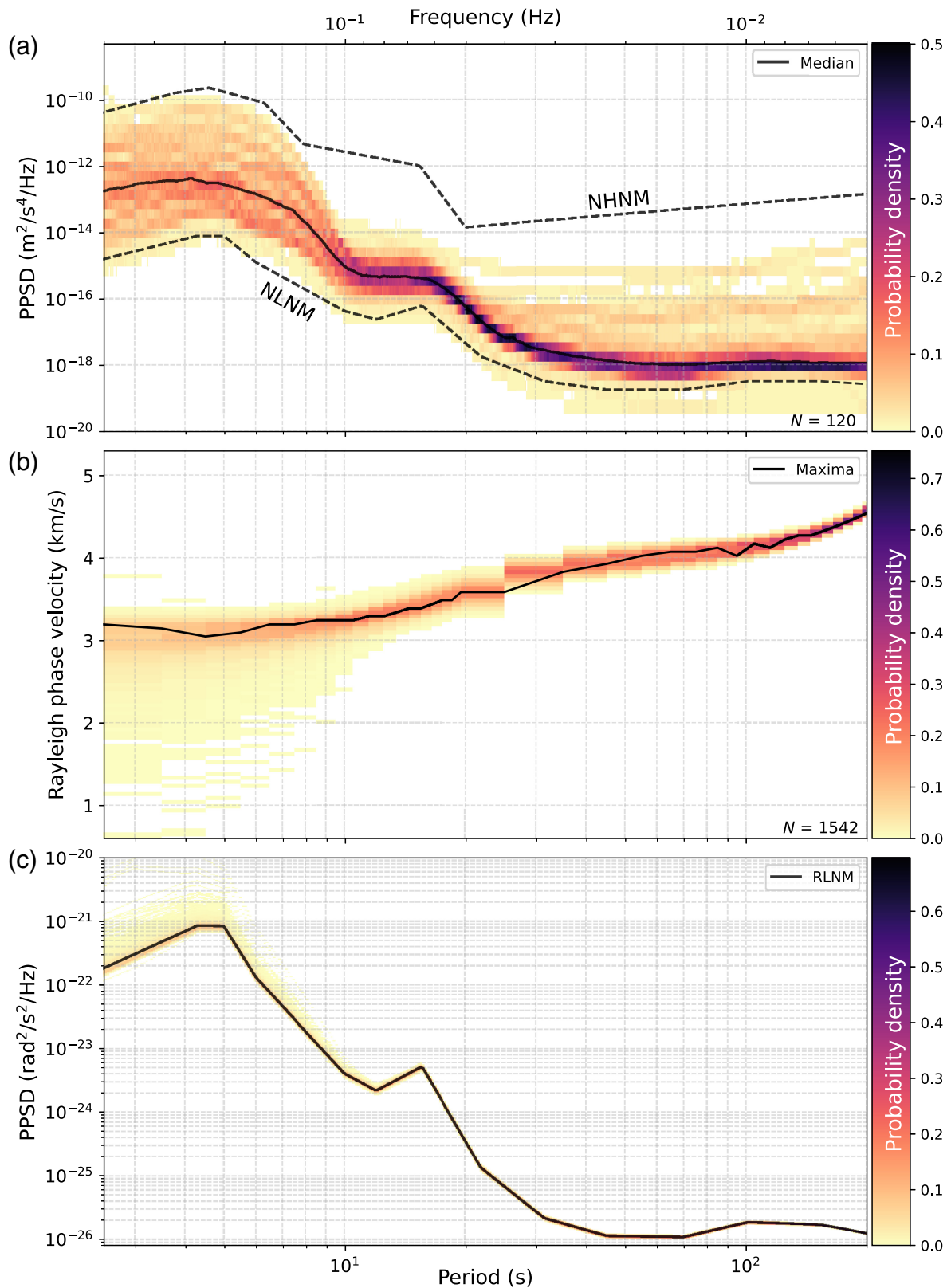
Figure 1. (a) The distribution of yearly median power spectral densities (PPSDs) for all stations shown in Figure. S6A color coded as a probability density with a computed median PSD, and the new low-noise model (NLNM) and new high-noise model (NHNM; black lines) by Peterson (1993). (b) The probability density of Rayleigh phase velocity curves at sampling locations shown in Figure S6b. The black line indicates the maximum of the distribution. (c) The estimated rotational low-noise models (RLNMs) based on the NLNM in panel (a) and the phase velocity curves in panel (b). The black solid line indicates the median RLNM. The color version of this figure is available only in the electronic edition.

Figure 2. The left panels show hourly power spectral densities for 2019 for the vertical component of (a) the ROMY ring laser in Fürstenfeldbruck, Germany; and (b) G-ring in Wettzell, Germany. The right panel represents the median of all PSDs (red solid line) with a 95% confidence interval (red shade). The black dashed line represents the RLNM. The color version of this figure is available only in the electronic edition.

interferometers). For this study, data of 2019 of the G-ring, located at the Geodetic Observatory in Wettzell (Germany; e.g., Schreiber *et al.,* 2006) and the vertical component of rotational motions in seismology (ROMY) ring laser array (Igel *et al.,* 2021), located at the Geophysical Observatory in Fürstenfeldbruck (Germany), are incorporated. Lasing in a horizontal plane, both the G-ring as well as the horizontal ring of ROMY are sensitive to rotations around a vertical axis. Hence, these rotational motions are induced by *SH*-polarized seismic waves (Love waves). The computed hourly PSDs for ROMY and G-ring of 2019 are shown in Figure 2. Gaps result from nonoperational periods and maintenance work. The secondary microseism is the dominating signal (2–10 s), with expected seasonal variation, yielding more energy in the winter months compared with the summer months (e.g., Tanimoto *et al.,* 2015).

Results

We convert the NLNM for vertical acceleration to a low-noise model for transverse rotations using equation (3). Figure 1c shows the obtained RLNMs as a probability density distribution

for a selected bandwidth of 2–200 s. The median of the distribution is selected and referred to hereafter as a theoretical RLNM. For the secondary microseism peak at ∼4–5 s, the RLNM yields a level of about 10^{-21} rad^2 s^2 Hz^{-1} and for the primary microseism peak (∼14 s) a level of about 5×10^{-24} rad^2 s^2 Hz^{-1}. The minimum rotational noise level is defined at 50–70 s with 10^{-26} rad^2 s^2 Hz^{-1}. For the secondary microseism, all three components of ADR of the PFO array show a smooth increase in power toward the peak with a steep drop toward 10 s (Fig. 3a). The peak for the secondary microseism shows an offset of about 2 s toward longer periods compared with the RLNM (Fig. 3a,b). Detailed investigations of this shift, observed at the PFO, is not within the scope of this article.
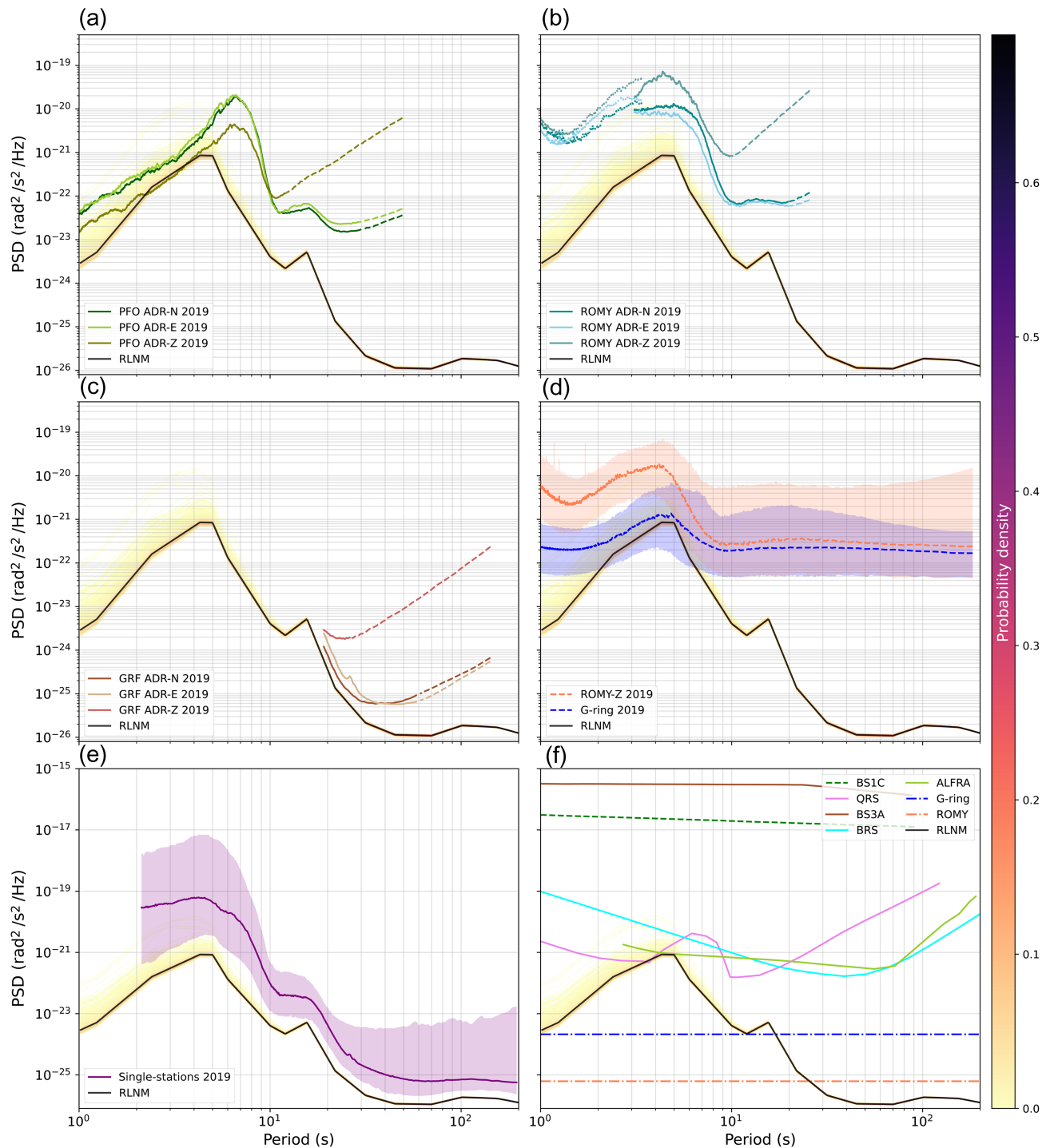
Figure 3. Inferred RLNMs are shown as a probability density distribution, and the median RLNM is plotted as a black, solid line. Compared are median PSDs of 2019 for three components of array-derived rotations (ADR) for (a) the Piñon Flats Observatory (PFO) array in California, U.S.A. (UC San Diego, 2014); (b) the outer (solid) and inner (dotted) ROMY (RMY) array in Fürstenfeldbruck, Germany; as well as (c) a subarray of the German Gräfenberg array (GRF; Federal Institute for Geosciences and Natural Resources, 1976), where fainted colors are outside the estimated usable frequency range of this array. The dotted lines toward longer periods for ADR indicate contamination by tilt predominantly by horizontal components, thus affecting vertical rotations the most. (d) The median PSDs of 2019 (dotted) and medians of selected days (solid) for vertical rotations of the large ring laser ROMY and G-Ring both located in Germany. The 90% confidence interval is shown as colored area, respectively. (e) A single-station model is based on median PSDs of 2019 of global seismic stations converted to rotations using local phase velocity profiles. (f) Compares self-noise levels of existing portable sensors BS3A (Bernauer et al., 2018), QRS (Venkateswara et al., 2021), BRS (Venkateswara et al., 2017), ALFRA (McCann et al., 2021; solid lines), a theoretical limit based on geometrical design only for large-scale ring lasers (ROMY and G-ring; dashed–dotted lines) and planned BS1C (Guattari, personal comm.; dashed line). The color version of this figure is available only in the electronic edition.

TABLE 1

Frequency Limits (f_{min} and f_{max}) and Set Period Limits (p_{min} and p_{max}) according to Equations (5) and (6) and Required Quantities (a = Aperture; c = Apparent Phase Velocity) for the Seismic Arrays: Piñon Flats Observatory Array (PFO), Gräfenberg Array (GRF), and ROMY Array (RMY; see Fig S1), Are Listed

Seismic Array	a (m)	c (km/s)	f_{min} (Hz)	f_{max} (Hz)	p_{min} (s)	p_{max} (s)
PFO	730	3.8	0.01	1.3	1.0	50.0
GRF	17851	3.8	0.006	0.05	18.8	156.6
RMY_o	2628	3.4	0.04	0.3	3.1	25.8
RMY_i	230	3.4	0.4	3.7	1.0	3.3

The RMY array is divided into an inner (RMY_i) and outer (RMY_o) subarray.

For the horizontal components, the peak of primary microseism is present with about one order of magnitude in power above the model (Fig. 3a). The ADR power spectra of the inner and outer RMY array show a broad peak for the secondary microseism band with approximately one order of magnitude in power higher (Fig. 3b). For the horizontal components, a signature of the primary microseism is present. The horizontal components of ADR for the GRF array follow the RLNM for periods within 18–70 s (Fig. 3c), supporting the estimated low-noise level for these periods. A continuation of the PSD outside the sensitive period band of the array (see Table 1) is indicated with dotted and dashed lines in Figure 3c. Median PSDs and a 95% confidence interval based on all PSDs of 2019 for G-ring and ROMY are shown in Figure 3d. For periods longer than 10 s, the optical Sagnac interferometers G-ring and ROMY approach a power level at $\sim 2 \times 10^{-22}$ rad^2 s^2 Hz^{-1} and 3×10^{-22} rad^2 s^2 Hz^{-1}, respectively. This limit is mainly controlled by optical losses of the optical resonator at the coated mirrors. Generally, more energy in the period band for secondary microseisms for ROMY compared with G-ring is most likely attributed to the geological setting of ROMY inside the pre-Alpine Molasse basin and its amplification characteristics.

Discussion
Validation of the RLNM
The NLNM and NHNM by Peterson (1993) have been influencing seismology in terms of better understanding Earth by quantifying its continuously excited noise level across frequencies, as well as a benchmark for instrument developers to provide instruments able to observe the smallest signals. If taken at face value, the RLNM is three to four orders of magnitude in power below the self-noise level of currently operating (portable) ground rotation sensors (see Fig. 3f), whereas at the same time self-noise level of today's broadband seismometers are below the NLNM in the studied period band. To close this gap and observe rotational ground motions at the level of the RLNM, major technical developments are still required. We provide the first estimate of the transverse RLNM for Earth based on a conversion of the NLNM for vertical

accelerations using globally distributed phase velocities of Rayleigh waves. The underlying assumptions are (1) that Rayleigh waves are the most energetic waves contributing to the seismic noise for periods between 2 and 200 s; and (2) the model-based phase velocities are representative. Concerning the latter assumption, the largest variations are at short period, and related to the crust and lithospheric lateral heterogeneities. We are using phase velocities derived from the recent global models. To convert vertical acceleration into transverse rotation with equation (3), it is assumed that most of the seismic energy corresponds to the Rayleigh waves as stated at the end of the Translation to rotation section as assumption 1. Ambient seismic noise in the 3–300 s period range is generated by ocean wave interactions with specific mechanisms depending on the period range (Hasselmann, 1963; Ardhuin et al., 2015). Secondary microseisms (period band: 3–10 s) are generated by ocean gravity wave–wave interactions and have been successfully modeled by considering the propagation of Rayleigh waves from the source regions to the stations (Stutzmann et al., 2012). Primary microseisms (period band: 10–20 s) are generated by ocean gravity waves interacting with the shallow ocean floor at the coast and can also be effectively modeled by considering only Rayleigh wave propagation (Gualtieri et al., 2019). Finally, the seismic hum with periods between 50 and 300 s was successfully modeled by considering ocean infragravity waves hitting continental shelves as source mechanisms and the propagation of Rayleigh waves (Deen et al., 2018). Most sources of seismic noise in the period range of 3–300 s originate from the ocean. Based on excitation by pressure loading at the ocean floor, Rayleigh waves are excited predominantly and polarized in the plane of propagation. However, Love waves, which have transverse polarization, have also been observed (e.g., Friedrich et al., 1998). Recently, Gualtieri et al. (2021) and Le Pape et al. (2021) showed that Love-wave constituents of secondary microseisms can be generated by Rayleigh-to-Love-wave conversion on a 3D interface close to the source region. An analysis of the average energy ratio of Rayleigh-to-Love waves for the secondary microseism including rotational measurements for the G-ring site in

Wettzell yields a range of 0.9–1.0 (Tanimoto *et al.*, 2015). For the site of PFO using seismic array data, energy ratios of 2.0–2.5 were obtained (Tanimoto *et al.*, 2016). For Japan, a ratio estimate of ∼2 was reported by Nishida *et al.* (2008). Although the Rayleigh-to-Love ratio is highly variable (Juretzek and Hadziioannou, 2016), it seems that considering only Rayleigh waves propagation serves a valid first-order approximation to support assumption 1 in the Translation to rotation section. To account for assumption 2, stated in the Translation to rotation section, on dispersive, global phase velocities for Love and Rayleigh waves, we relied on up-to-date crustal and upper-mantle models and employed median velocities to suppress local effects of the globally sampled velocities.

The median and confidence interval of the single-station estimate based on local rotational models is compared with the RLNM in Figure 3e. The overall characteristics of the model are reflected, however with an overall higher power level, that we attribute mostly to station quality.

ADR data of three arrays support the RLNM for their respective frequency range. An increase in power toward longer periods is observed for all ADR data, which can be attributed to a dominating influence of amplitude noise for longer periods affecting derived gradients. For all arrays, the vertical ADR spectra show higher noise levels compared with the horizontal ones. Generally, horizontal components of translational records are more noisy.

Large-scale ring lasers currently provide the best direct, high-sensitive measurement of rotational round motions. However, a nonportable ring laser is not directly comparable with portable sensors, neither in design, nor operation effort or operation costs. A theoretical sensitivity limit, for the large-scale ring lasers G-ring and ROMY, respectively, is shown in Figure 3f. This resolution or sensitivity limit is merely taking into account the geometrical design of the ring, therefore, defining a pure theoretical limit. We neglect limitations due to noise sources (e.g., lasing process, electronic self-noise, or cavity losses at the mirrors). The dominant limitation defining in the current observation levels (see Fig. 3d) is dominated by the scattering, transmission, and absorption losses at the coated mirrors of the resonator cavity.

Fibre-optic rotational rate sensors, such as the blueSeis-3A sensor (BS3A; Bernauer *et al.*, 2018) or the planned blueSeis-1C sensor (BS1C; personal comm.), already offer many field applications based on rotational sensing; however, their instrumental self-noise levels are still 2–4 orders of magnitude in power above the presented RLNM. Self-noise characteristics of three mechanical beam balances under development for horizontal components, namely, ALFRA (McCann *et al.*, 2021), QRS (Venkateswara *et al.*, 2021), and BRS (Venkateswara *et al.*, 2017), are shown in Figure 3f. With regard to the QRS sensor, the presented self-noise level is inferred from observations in a vault (Venkateswara *et al.*, 2021), which seemed to reveal some power in the secondary microseism band. For the secondary

microseisms range (2–10 s), a reduction of the self-noise level for BRS, QRS, and ALFRA of about one to two orders of magnitude in power would be sufficient to resolve signals at the RLNM. Still two to three orders of magnitude in power of reduction is required for periods above about 20 s.

To gain access to the full dynamic range of rotational signals, the self-noise levels of these sensors have to be further reduced below the RLNM for the seismically active frequency range between 2 and 100 s (10 mHz–0.5 Hz).
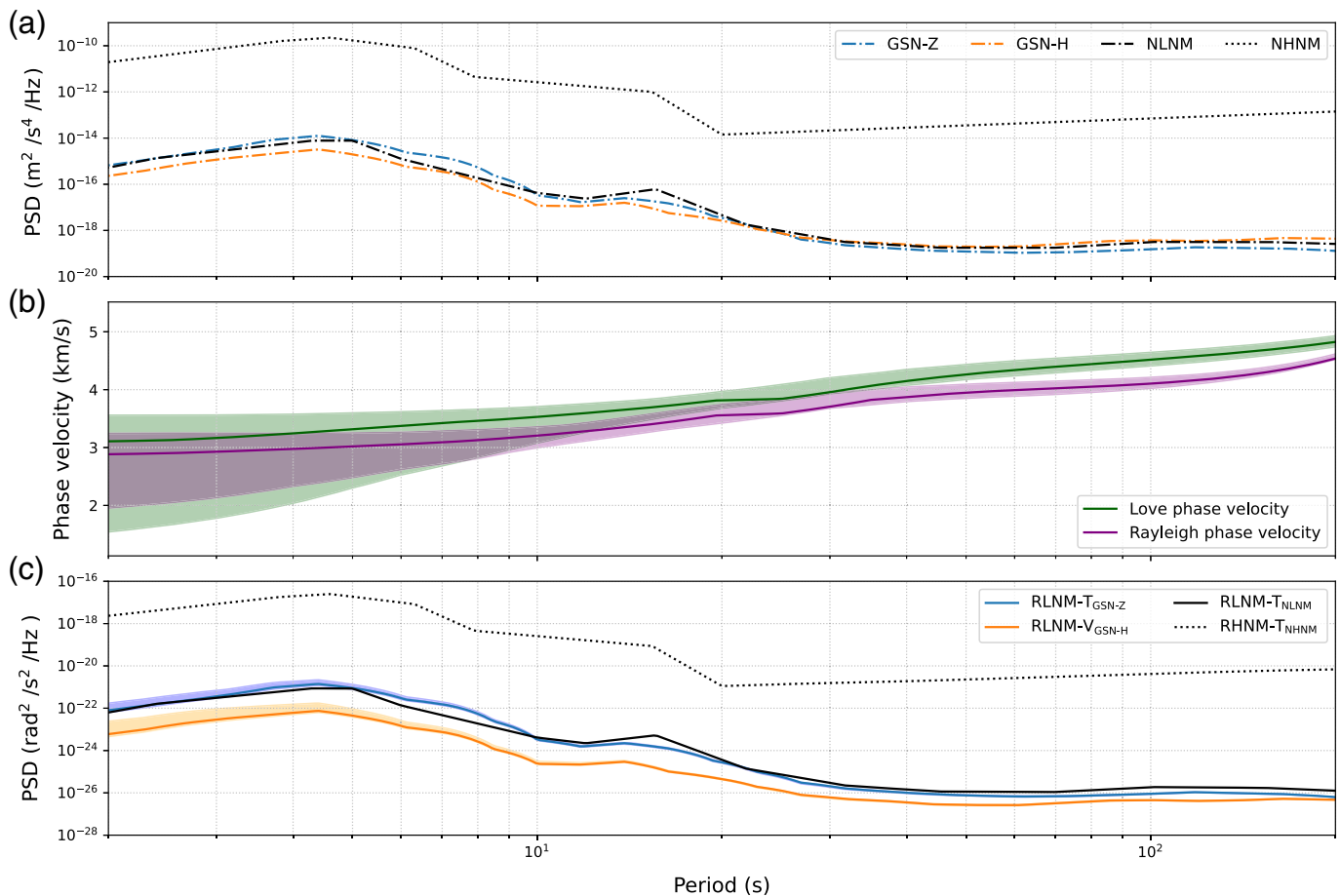
Comparison of NLNM and GSN low-noise models

We decided to focus on the NLNM by Peterson (1993) as a well-cited benchmark for vertical seismic acceleration observations. Other low-noise models, based on data of the Global Seismic Network (GSN) for vertical (GSN-Z) and also horizontal (GSN-H) accelerations, introduced by Berger *et al.* (2004), are converted to rotational models in Figure 4 for comparison purposes. The GSN-Z model only shows minor deviations from the NLNM, thus the converted transverse RLNMs of $RLNM - T_{NLNM}$ and $RLNM - T_{GSN-Z}$, respectively, match well.

For the conversion, an assumption of dominantly first-order Rayleigh wave energy for vertical component for the investigated frequency bandwidth has been made and discussed. To convert the GSN-H noise model to rotational rates, an assumption of dominantly Love-wave energy would be required. This would be a very strong assumption, when assuming equipartitioning of Love-wave and horizontal Rayleigh-wave energy. Nevertheless, we include the conversion of the GSN-H model for horizontal accelerations using Love phase velocities (see Fig. 4b) according to equation (2). The resulting model ($RLNM - V_{GSN-H}$) shows a noise level for vertical rotations of about one order of magnitude in power lower compared with transverse rotations while converging toward longer periods (Fig. 4c). This resembles the characteristics for horizontal acceleration noise levels, being lower for the microseisms bands and higher toward longer periods, in comparison with vertical acceleration noise models (Fig. 4a). For the range of 2–20 s, the GSN-H model suggests a lower noise floor for horizontal accelerations with respect to vertical accelerations. Because vertical rotations are induced by horizontal motions, we assume the noise floor of a vertical RLNM to be rather lower than higher with regard to the transverse RLNM for the respective period band. Although we consider the assumptions for the derivation of the transverse RLNM to be on solid ground, we acknowledge that the assumptions that went into the construction of the vertical RLNM are not. Therefore, we simply propose that the former model should be taken as a benchmark for both types of rotations until better constrained vertical RLNM models become available.

Toward long periods

The proposed low-noise model for rotational ground motions is restricted by the discussed assumptions, in particular,

Figure 4. (a) Translational low-noise models for ground acceleration: the new low- and high-noise models (NLNM and NHNM) by Peterson (1993), as well as the horizontal (GSN-H) and the vertical (GSN-Z) low-noise model based on data of the Global Seismic Network (GSN) by Berger et al. (2004). (b) The phase velocities for Rayleigh and Love waves are shown, including a 95% confidence interval. (c) The corresponding low-noise models for transverse (-T) and vertical (-V) rotational motions according to equations (2) and (3). Here we assume that the GSN-Z noise is predominantly composed of Rayleigh waves, whereas the GSN-H noise is predominantly made up of Love waves, being aware that the latter assumption of equipartitioning is a very strong assumption. The color version of this figure is available only in the electronic edition.

concerning the period range. Toward long periods above 200–300 s locally generated noise resulting from atmospheric movement above the station starts to dominate seismic far-field signals, such as spheroidal and toroidal hum introduced rotations. Those influences are likely pronounced differently for vertical and transversal rotational components. For vertical and horizontal rotational observations at long periods, we expect a different level in analogy to translational observations, because local processes, such as atmospheric pressure-induced ground tilts, influence vertical and horizontal components differently.

Conclusions

We propose a (transverse) RLNM based on the NLNM by Peterson (1993) for vertical accelerations, assuming dominantly Rayleigh-wave type energy across a period range of 2–200 s. The conversion is based on surface-wave velocities extracted from state of the art lithospheric seismic velocity models. A comparison with GSN low-noise models for accelerations by Berger et al. (2004) reveals a lower noise level for vertical rotations of about one magnitude in power, however, requiring a strong assumption of equipartitioning for the conversion. We expect different levels for transverse and vertical rotation noise floors, but we propose that the transverse RLNM is taken as a benchmark for both types of rotations until better constrained vertical RLNM models become available.

To validate the RLNM with currently available observations, we used array-derived rotations (ADR) from three differently sized seismic arrays and direct rotational measurements of the large-scale ring lasers, G-ring and ROMY, over the entire year of 2019. All observational data are compatible with the inferred background noise level for rotations of the RLNM for their representative period bands.

Self-noise levels of state-of-the-art rotational sensors, either already operational or still under development, are compared against the RLNM. Large-scale, high-sensitive ring lasers, such as G-ring and ROMY, approach the RLNM, in particular, at

the secondary microseism peak. Lowering the currently limiting self-noise levels for these ring lasers requires technical improvements, especially for the coated corner mirrors to reduce losses of the optical cavity.

Available portable rotational sensors (e.g., blueSeis-3A, ALFRA, and QRS) already provide a sensitivity level sufficient for a wide range of geophysical applications or seismic isolation (e.g., gravitational wave detectors). However, none of these sensors has currently a self-noise level below the proposed RLNM. Although lowering self-noise levels of rotational sensors below the RLNM remains technically challenging, it is nevertheless essential to achieve this goal to extend the domain of applications to that currently possible with classic seismometers.

Data and Resources

Data of the Ring laser ROMY and its seismic array were provided by the Geophysical observatory in Fürstenfeldbruck (Department of Earth and Environmental Sciences, Geophysical Observatory, University of Munich, 2001). Data of the G-ring were provided by the Geodetic observatory in Wettzell. Data of the Piñon Flats Observatory array (UC San Diego, 2014) and the Gräfenberg array (Federal Institute for Geosciences and Natural Resources, 1976) are openly accessible via Incorporated Research Institutions for Seismology (IRIS) and BGR International Federation of Digital Seismograph Networks (FDSN) services, respectively. Data of the Global Seismograph Network II (Scripps Institution of Oceanography, 1986), Global Seismograph Network (GSN) IU (Albuquerque Seismological Laboratory/U.S. Geological Survey [USGS], 2014), and GEOSCOPE network G (Institut de physique du globe de Paris [IPGP] and École et Observatoire des Sciences de la Terre de Strasbourg [EOST], 1982) went into the analysis, and the free availability is acknowledged. Extensive parts of data processing were done using modules of the ObsPy Python package (Megies et al., 2011). Phase velocities are computed using the model from Haned et al. (2016). GSN noise model data are based on Berger et al. (2004). All other data used in this article came from the published sources listed in the references. The supplemental material includes a more detailed background for the equations presented in the Methodology section and additional figures related to the observational data used for comparison with the rotational low-noise model (RLNM). Data repository: Data files of the transverse RLNM as well as Jupyter notebooks to recreate the figures of this article are available at https://github.com/andbrocode/RotationalLowNoiseModel.git; doi: 10.5281/zenodo.10027880; and https://syncandshare.lrz.de/getlink/fiGtpiKTn9cmUtHixKqP1A/SRL-RLNM-2023. All websites were last accessed in December 2023. For more information, please contact the first author.

Declaration of Competing Interests

The authors acknowledge that there are no conflicts of interest recorded.

Acknowledgments

References

Aki, K., and P. G. Richards (2002). Quantitative Seismology, University Science Books, Sausalito, California, U.S.A.

Albuquerque Seismological Laboratory/U.S. Geological Survey (USGS) (2014). Global seismograph network, GSN - IRIS/USGS, doi: 10.7914/SN/IU.

Ardhuin, F., L. Gualtieri, and E. Stutzmann (2015). How ocean waves rock the earth: Two mechanisms explain microseisms with periods 3 to 300 s, Geophys. Res. Lett. 42, 765–772, doi: 10.1002/2014GL062782.

Belfi, J., N. Beverini, G. Carelli, A. Di Virgilio, E. Maccioni, G. Saccorotti, F. Stefani, and A. Velikoseltsev (2012). Horizontal rotation signals detected by "g-pisa" ring laser for the M_w 9.0, March 2011, Japan earthquake, J. Seismol. 16, 767–776, doi: 10.1007/s10950-012-9276-9.

Berger, J., P. Davis, and G. Ekström (2004). Ambient earth noise: A survey of the global seismographic network, J. Geophys. Res. 109, doi: 10.1029/2004JB003408.

Bernauer, F., J. Wassermann, F. Guattari, A. Frenois, A. Bigueur, A. Gaillot, E. de Toldi, D. Ponceau, U. Schreiber, and H. Igel (2018). BlueSeis3A: Full characterization of a 3C broadband rotational seismometer, Seismol. Res. Lett. 89, 620–629, doi: 10.1785/0220170143.

Bernauer, F., J. Wassermann, and H. Igel (2012). Rotational sensors—A comparison of different sensor types, J. Seismol. 16, 595–602, doi: 10.1007/s10950-012-9286-7.

Bernauer, F., J. Wassermann, and H. Igel (2020). Dynamic tilt correction using direct rotational motion measurements, Seismol. Res. Lett. 91, 2872–2880, doi: 10.1785/0220200132.

Brune, J. N., and J. Oliver (1959). The seismic noise of the Earth's surface, Bull. Seismol. Soc. Am. 49, 349–353, doi: 10.1785/BSSA0490040349.

Cochard, A., H. Igel, B. Schuberth, W. Suryanto, A. Velikoseltsev, U. Schreiber, J. Wassermann, F. Scherbaum, and D. Vollmer (2006). Rotational motions in seismology: Theory, observation, simulation, in Earthquake Source Asymmetry, Structural Media and Rotation Effects, R. Teisseyre, E. Majewski, and M. Takeo (Editors), Springer, Berlin, Heidelberg, 391–411.

Deen, M., E. Stutzmann, and F. Ardhuin (2018). The earth's hum variations from a global model and seismic recordings around the Indian Ocean, Geochem. Geophys. Geosys. 19, 4006–4020, doi: 10.1029/2018GC007478.

Department of Earth and Environmental Sciences, Geophysical Observatory, University of Munich (2001). BayernNetz, available at https://www.fdsn.org/networks/detail/BW/ (last accessed December 2023).

Donner, S., M. Bernauer, and H. Igel (2016). Inversion for seismic moment tensors combining translational and rotational ground motions, Geophys. J. Int. 207, 562–570, doi: 10.1093/gji/ggw298.

Donner, S., C. Lin, C. Hadziioannou, A. Gebauer, F. Vernon, D. C. Agnew, H. Igel, U. Schreiber, and J. Wassermann (2017).

Comparing direct observation of strain, rotation, and displacement with array estimates at Piñon flat observatory, California, *Seismol. Res. Lett.* **88,** 1107–1116, doi: 10.1785/0220160216.

Federal Institute for Geosciences and Natural Resources (1976). German Regional Seismic Network (GRSN), available at https://www.seismologie.bgr.de/doi/grsn/, doi: 10.25928/MBX6-HR74.

Friedrich, A., F. Krüger, and K. Klinge (1998). Ocean-generated microseismic noise located with the Gräfenberg array, *J. Seismol.* **2,** 47–64, doi: 10.1023/A:1009788904007.

Gualtieri, L., E. Bachmann, F. J. Simons, and J. Tromp (2021). Generation of secondary microseism love waves: effects of bathymetry, 3-d structure and source seasonality, *Geophys. J. Int.* **226,** 192–219, doi: 10.1093/gji/ggab095.

Gualtieri, L., E. Stutzmann, C. Juretzek, C. Hadziioannou, and F. Ardhuin (2019). Global scale analysis and modelling of primary microseisms, *Geophys. J. Int.* **218,** 560–572, doi: 10.1093/gji/ggz161.

Guéguen, P., and A. Astorga (2021). The torsional response of civil engineering structures during earthquake from an observational point of view, *Sensors* **21,** 342, doi: 10.3390/s21020342.

Hadziioannou, C., P. Gaebler, U. Schreiber, J. Wassermann, and H. Igel (2012). Examining ambient noise using colocated measurements of rotational and translational motion, *J. Seismol.* **16,** 787–796, doi: 10.1007/s10950-012-9288-5.

Haned, A., E. Stutzmann, M. Schimmel, S. Kiselev, A. Davaille, and A. Yelles-Chaouche (2016). Global tomography using seismic hum, *Geophys. J. Int.* **204,** 1222–1236, doi: 10.1093/gji/ggv516.

Hasselmann, K. (1963). A statistical analysis of the generation of microseisms, *Rev. Geophys.* **1,** 177–210, doi: 10.1029/RG001i002p00177.

Huang, B. S. (2003). Ground rotational motions of the 1999 Chi-Chi, Taiwan earthquake as inferred from dense array observations, *Geophys. Res. Lett.* **30,** doi: 10.1029/2002GL015157.

Igel, H., A. Cochard, J. Wassermann, A. Flaws, U. Schreiber, A. Velikoseltsev, and N. Dinh Pham (2007). Broad-band observations of earthquake-induced rotational ground motions, *Geophys. J. Int.* **168,** 182–196, doi: 10.1111/j.1365-246X.2006.03146.x.

Igel, H., M. F. Nader, D. Kurrle, A. M. Ferreira, J. Wassermann, and K. U. Schreiber (2011). Observations of Earth's toroidal free oscillations with a rotation sensor: The 2011 magnitude 9.0 Tohoku-Oki earthquake, *Geophys. Res. Lett.* **38,** doi: 10.1029/2011GL049045.

Igel, H., K. U. Schreiber, A. Gebauer, F. Bernauer, S. Egdorf, A. Simonelli, C. J. Lin, J. Wassermann, S. Donner, C. Hadziioannou, *et al.* (2021). ROMY: A multicomponent ring laser for geodesy and geophysics, *Geophys. Res. Lett.* **225,** 684–698, doi: 10.1093/gji/ggaa614.

Igel, H., U. Schreiber, A. Flaws, B. Schuberth, A. Velikoseltsev, and A. Cochard (2005). Rotational motions induced by the M 8. 1 Tokachi-oki earthquake, September 25, 2003, *Geophys. Res. Lett.* **32,** doi: 10.1029/2004GL022336.

Institut de physique du globe de Paris (IPGP), École et Observatoire des Sciences de la Terre de Strasbourg (EOST) (1982). Geoscope, French global network of broad band seismic stations, doi: 10.18715/GEOSCOPE.G.

Juretzek, C., and C. Hadziioannou (2016). Where do ocean microseisms come from? A study of love-to-Rayleigh wave ratios, *J. Geophys. Res.* **121,** 6741–6756, doi: 10.1002/2016JB013017.

Keil, S., J. Wassermann, and H. Igel (2021). Single-station seismic microzonation using 6C measurements. *J. Seismol.* **25,** 103–114, doi: 10.1007/s10950-020-09944-1.

Kislov, K., and V. Gravirov (2021). Rotational seismology: Review of achievements and outlooks, *Seismic Instrum.* **57,** 187–202, doi: 10.3103/S0747923921020262.

Laske, G., G. Masters, Z. Ma, and M. Pasyanos. (2013). Update on CRUST1.0 - A 1-degree global model of Earth's crust, *Geophys. Res. Abstracts*, 7–12 April 2013, Vienna, Austria, Abstract EGU2013-2658, available at http://igppweb.ucsd.edu/~gabi/crust1.html.

Le Pape, F., D. raig, and C. J. Bean (2021). How deep ocean-land coupling controls the generation of secondary microseism love waves, *Nat. Commun.* **12,** 2332, doi: 10.1038/s41467-021-22591-5.

Leugoud, R., and A. Kharlamov (2012). Second generation of a rotational electrochemical seismometer using magnetohydrodynamic technology, *J. Seismol.* **16,** 587–593, doi: 10.1007/s10950-012-9290-y.

Liao, C. M., K. Hicke, F. Bernauer, H. Igel, C. Hadziioannou, and E. Niederleithinger (2022). Multi-sensor measurements on a large-scale bridge model, in *5. Brückenkolloquium: Fachtagung für Beurteilung, Planung, Bau, Instandhaltung und Betrieb von Brücken*, 6–7 September 2022, Ostfildern, Germany, 223.

Lin, C. J., H. P. Huang, N. D. Pham, C. C. Liu, W. C. Chi, and W. H. Lee (2011). Rotational motions for teleseismic surface waves, *Geophys. Res. Lett.* **38,** doi: 10.1029/2011GL047959.

Lindner, F., J. Wassermann, M. C. AurschSchmidt-, K. U. Schreiber, and H. Igel (2017). Seafloor ground rotation observations: Potential for improving signal-to-noise ratio on horizontal OBS components, *Seismol. Res. Lett.* **88,** 32–38, doi: 10.1785/0220160051.

McCann, J. J., J. Winterflood, L. Ju, and C. Zhao (2021). A multi-orientation low-frequency rotational accelerometer, *Rev. Sci. Instrum.* **92,** 064,503, doi: 10.1063/5.0047069.

McLeod, D., G. Stedman, T. Webb, and U. Schreiber (1998). Comparison of standard and ring laser rotational seismograms, *Bull. Seismol. Soc. Am.* **88,** 1495–1503, doi: 10.1785/BSSA0880061495.

Megies, T., M. Beyreuther, R. Barsch, L. Krischer, and J. Wassermann (2011). ObsPy–What can it do for data centers and observatories? *Ann. Geophys.* **54,** 47–58.

Nader, M., H. Igel, A. Ferreira, D. Al-Attar, J. Wassermann, and K. Schreiber (2015). Normal mode coupling observations with a rotation sensor, *Geophys. J. Int.* **201,** 1482–1490, doi: 10.1093/gji/ggv082.

Nishida, K., H. Kawakatsu, Y. Fukao, and K. Obara (2008). Background Love and Rayleigh waves simultaneously generated at the Pacific ocean floors, *Geophys. Res. Lett.* **35,** doi: 10.1029/2008GL034753.

Noe, S., S. Yuan, J. P. Montagner, and H. Igel (2022). Anisotropic elastic parameter estimation from multicomponent ground-motion observations: A theoretical study, *Geophys. J. Int.* **229,** 1462–1473, doi: 10.1093/gji/ggac006.

Ortolan, A., J. Belfi, F. Bosi, A. Di Virgilio, N. Beverini, G. Carelli, E. Maccioni, R. Santagata, A. Simonelli, A. Beghi, *et al.* (2016). The GINGER project and status of the GINGERino prototype at LNGS, in *Journal of Physics: Conference Series*, IOP Publishing, 072,003 pp., doi: 10.1088/1742-6596/718/7/072003.

Pancha, A., T. H. Webb, G. E. Stedman, D. P. McLeod, and K. U. Schreiber (2000). Ring laser detection of rotations from teleseismic waves, *Geophys. Res. Lett.* **27,** 3553–3556, doi: 10.1029/2000GL011734.

Peterson, J. R. (1993). Observations and modeling of seismic background noise, *U.S. Geol. Surv. Open-File Rept. 93–322*, doi: 10.3133/ofr93322.

Poppeliers, C., and E. V. Evans (2015). The effects of measurement uncertainties in seismic-wave gradiometry, *Bull. Seismol. Soc. Am.* **105,** 3143–3155, doi: 10.1785/0120150043.

Saito, M. (1988). DISPER80: A subroutine package for the calculation of seismic normal mode solutions, in *Seismological Algorithms: Computational Methods and Computer Programs*, D. J. Doornbos (Editor), Academic Press, New York, 293–319, doi: 10.3124/segj.64.127.

Schmelzbach, C., S. Donner, H. Igel, D. Sollberger, T. Taufiqurrahman, F. Bernauer, M. Häusler, C. Van Renterghem, J. Wassermann, and J. Robertsson (2018). Advances in 6c seismology: Applications of combined translational and rotational motion measurements in global and exploration seismology, *Geophysics* **83,** 53–69, doi: 10.1190/geo2017-0492.1.

Schreiber, U., and J. P. Wells (2023). *Rotation Sensing with Large Ring Lasers: Applications in Geophysics and Geodesy*, Cambridge University Press, Cambridge, United Kingdom, doi: 10.1017/9781108524933.

Schreiber, K. U., G. E. Stedman, H. Igel, and A. Flaws (2006). Ring laser gyroscopes as rotation sensors for seismic wave studies, in *Earthquake Source Asymmetry, Structural Media and Rotation Effects*, Teisseyre, R., E. Majewski, and M. Takeo (Editors), Springer, 377–390.

Scripps Institution of Oceanography (1986). Global seismograph network, IRIS/IDA, doi: 10.7914/SN/II.

Singh, S., Y. Capdeville, and H. Igel (2020). Correcting wavefield gradients for the effects of local small-scale heterogeneities, *Geophys. J. Int.* **220,** 996–1011, doi: 10.1093/gji/ggz479.

Sollberger, D., H. Igel, C. Schmelzbach, P. Edme, D. J. Van Manen, F. Bernauer, S. Yuan, J. Wassermann, U. Schreiber, and J. O. Robertsson (2020). Seismological processing of six degree-of-freedom ground-motion data, *Sensors* **20,** 6904, doi: 10.3390/s20236904.

Spudich, P., and J. B. Fletcher (2008). Observation and prediction of dynamic ground strains, tilts, and torsions caused by the Mw6.0 2004 Parkfield, California, earthquake and aftershocks, derived from UPSAR array observations, *Bull. Seismol. Soc. Am.* **98,** 1898–1914, doi: 10.1785/0120070157.

Stedman, G., Z. Li, and H. Bilger (1995). Sideband analysis and seismic detection in a large ring laser, *Appl. Opt.* **34,** 5375–5385, doi: 10.1364/AO.34.005375.

Stutzmann, E., F. Ardhuin, M. Schimmel, A. Mangeney, and G. Patau (2012). Modelling long-term seismic noise in various environments, *Geophys. J. Int.* **191,** 707–722, doi: 10.1111/j.1365-246X.2012.05638.x.

Suryanto, W., H. Igel, J. Wassermann, A. Cochard, B. Schuberth, D. Vollmer, F. Scherbaum, U. Schreiber, and A. Velikoseltsev (2006). First comparison of array-derived rotational ground motions with direct ring laser measurements, *Bull. Seismol. Soc. Am.* **96,** 2059–2071, doi: 10.1785/0120060004.

Tang, L., H. Igel, and J.-P. Montagner (2023). Single-point dispersion measurement of surface waves combining translation, rotation and strain in weakly anisotropic media: Theory, *Geophys. J. Int.* **235,** 24–47, doi: 10.1093/gji/ggad199.

Tanimoto, T., C. Hadziioannou, H. Igel, J. Wasserman, U. Schreiber, and A. Gebauer (2015). Estimate of Rayleigh-to-Love wave ratio in the secondary microseism by colocated ring laser and seismograph, *Geophys. Res. Lett.* **42,** 2650–2655, doi: 10.1002/2015GL063637.

Tanimoto, T., C. J. Lin, C. Hadziioannou, H. Igel, and F. Vernon (2016). Estimate of Rayleigh-to-Love wave ratio in the secondary microseism by a small array at Piñon Flats Observatory, California, *Geophys. Res. Lett.* **43,** 11–173, doi: 10.1002/2016GL071133.

Todd, K. (2020). toddkarin/global-land-mask: Release of version 1.0.0, doi: 10.5281/zenodo.4066722.

UC San Diego (2014). Piñon flats observatory array, available at https://www.fdsn.org/networks/detail/PY/ (last accessed December 2023).

Venkateswara, K., C. A. Hagedorn, J. H. Gundlach, J. Kissel, J. Warner, H. Radkins, T. Shaffer, B. Lantz, R. Mittleman, F. Matichard, *et al.* (2017). Subtracting tilt from a horizontal seismometer using a ground-rotation sensor, *Bull. Seismol. Soc. Am.* **107,** 709–717, doi: 10.1785/0120160310.

Venkateswara, K., J. Paros, P. Bodin, W. Wilcock, and H. J. Tobin (2021). Rotational seismology with a quartz rotation sensor, *Seismol. Res. Lett.* **93,** 173–180, doi: 10.1785/0220210171.

Wassermann, J., S. Lehndorfer, H. Igel, and U. Schreiber (2009). Performance test of a commercial rotational motions sensor, *Bull. Seismol. Soc. Am.* **99,** 1449–1456, doi: 10.1785/0120080157.

Yuan, S., A. Simonelli, C. J. Lin, F. Bernauer, S. Donner, T. Braun, J. Wassermann, and H. Igel (2020). Six degree-of-freedom broadband ground-motion observations with portable sensors: Validation, local earthquakes, and signal processing, *Bull. Seismol. Soc. Am.* **110,** 953–969, doi: 10.1785/0120190277.

Zembaty, Z., F. Bernauer, H. Igel, and K. U. Schreiber (2021). Rotation rate sensors and their applications, *Sensors* **21,** no. 16, 5344, doi: 10.3390/s21165344.